Research Article | Vol. 8, No. 11 | 1 Nov 2017 | BIOMEDICAL OPTICS EXPRESS 5001
Biomedical Optics EXPRESS

Noninvasive structural and microvascular anatomy of oral mucosae using handheld optical coherence tomography

MENG-TSAN TSAI,[1,2,3] YINGDAN CHEN,[2,4] CHENG-YU LEE,[1] BO-HUEI HUANG,[1] NGUYEN HOANG TRUNG,[1] YA-JU LEE,[5,*] AND YEN-LI WANG[6,7,8]

[1]*Department of Electrical Engineering, Chang Gung University, Taoyuan, 33302 Taiwan*
[2]*Medical Imaging Research Center, Institute for Radiological Research, Chang Gung University and Chang Gung Memorial Hospital at Linkou, Taoyuan, 33302 Taiwan*
[3]*Department of Dermatology, Chang Gung Memorial Hospital, Linkou, 33305 Taiwan*
[4]*School of Information and Electronic Engineering, Zhejiang Gongshang University, Hangzhou, 31108 China*
[5]*Institute of Electro-Optical Science and Technology, National Taiwan Normal University, 11677 Taiwan*
[6]*Department of Periodontics, Chang Gung Memorial Hospital, Taoyuan, 33378 Taiwan*
[7]*College of Medicine, Chang Gung University, Taoyuan, 33302 Taiwan*
[8]*m5975@cgmh.org.tw*
[*]*yajulee@ntnu.edu.tw*

Abstract: In this study, we demonstrated the feasibility of using a handheld optical coherence tomography (OCT) for *in vivo* visualizations of the microstructural and microvascular features of various oral mucosal types. To scan arbitrary locations of the oral mucosa, a scanning probe was developed, composed of a probe body fabricated by a 3D printer, miniaturized two-axis galvanometer, relay lenses, and reflective prism. With a 3D printing technique, the probe weight and the system volume were greatly reduced, enabling the effective improvement of imaging artifacts from unconscious motion and system complexity. Additionally, in our design, the distal end of the probe can be switched to fit various oral conditions, and the optical parameters of the probe, such as the transverse resolution, working distance, and probe length can be easily varied. The results showed that the epithelium and lamina propria layers, as well as the fungiform papilla and salivary gland, were differentiated. Moreover, various microcirculation features at different mucosal sites were identified that are potentially effective indicators for the diagnosis of premalignant lesions. The demonstrated results indicate that the developed OCT system is a promising tool for noninvasive imaging of oral mucosae.

OCIS codes: (170.4500) Optical coherence tomography; (170.2655) Functional monitoring and imaging; (170.3880) Medical and biological imaging.

References and links

1. R. L. Siegel, K. D. Miller, and A. Jemal, "Cancer statistics, 2015," CA Cancer J. Clin. **65**(1), 5–29 (2015).
2. C. A. Squier and M. J. Kremer, "Biology of Oral Mucosa and Esophagus," J. Natl. Cancer Inst. Monogr. **2001**(29), 7–15 (2001).
3. B. Neville, D. D. Damm, C. Allen, and J. Bouquot, Oral and Maxillofacial Pathology. 3rd Edition. (Saunders, 2008).
4. G. W. Gynther, B. Rozell, and A. Heimdahl, "Direct oral microscopy and its value in diagnosing mucosal lesions: A pilot study," Oral Surg. Oral Med. Oral Pathol. Oral Radiol. Endod. **90**(2), 164–170 (2000).
5. L. L. Gleich, P. W. Biddinger, Z. P. Pavelic, and J. L. Gluckman, "Tumor angiogenesis in T1 oral cavity squamous cell carcinoma: Role in predicting tumor aggressiveness," Head Neck **18**(4), 343–346 (1996).
6. L. L. Gleich, P. W. Biddinger, F. D. Duperier, and J. L. Gluckman, "Tumor angiogenesis as a prognostic indicator in T2-T4 oral cavity squamous cell carcinoma: A clinical-pathologic correlation," Head Neck **19**(4), 276–280 (1997).
7. S. Silverman, Jr., "Early diagnosis of oral cancer," Cancer **62**(8 Suppl), 1796–1799 (1988).

#304829 https://doi.org/10.1364/BOE.8.005001
Journal © 2017 Received 15 Aug 2017; revised 26 Sep 2017; accepted 9 Oct 2017; published 13 Oct 2017

Biomedical Optics EXPRESS

8. M. Lingen, E. M. Sturgis, and M. S. Kies, "Squamous cell carcinoma of the head and neck in nonsmokers: clinical and biologic characteristics and implications for management," Curr. Opin. Oncol. **13**(3), 176–182 (2001).
9. M. R. Tsai, D. B. Shieh, P. J. Lou, C. F. Lin, and C. K. Sun, "Characterization of oral squamous cell carcinoma based on higher-harmonic generation microscopy," J. Biophotonics **5**(5-6), 415–424 (2012).
10. A. G. Ammer, K. E. Hayes, K. H. Martin, L. Zhang, G. A. Spirou, and S. A. Weed, "Multi-photon imaging of tumor cell invasion in an orthotopic mouse model of oral squamous cell carcinoma," J. Vis. Exp. **53**, e2941 (2011).
11. P. Wilder-Smith, T. Krasieva, W. G. Jung, J. Zhang, Z. Chen, K. Osann, and B. Tromberg, "Noninvasive imaging of oral premalignancy and malignancy," J. Biomed. Opt. **10**(5), 051601 (2005).
12. A. L. Clark, A. M. Gillenwater, T. G. Collier, R. Alizadeh-Naderi, A. K. El-Naggar, and R. R. Richards-Kortum, "Confocal Microscopy for Real-Time Detection of Oral Cavity Neoplasia," Clin. Cancer Res. **9**(13), 4714–4721 (2003).
13. J. M. Jabbour, J. L. Bentley, B. H. Malik, J. Nemechek, J. Warda, R. Cuenca, S. Cheng, J. A. Jo, and K. C. Maitland, "Reflectance confocal endomicroscope with optical axial scanning for in vivo imaging of the oral mucosa," Biomed. Opt. Express **5**(11), 3781–3791 (2014).
14. H. Fatakdawala, S. Poti, F. Zhou, Y. Sun, J. Bec, J. Liu, D. R. Yankelevich, S. P. Tinling, R. F. Gandour-Edwards, D. G. Farwell, and L. Marcu, "Multimodal in vivo imaging of oral cancer using fluorescence lifetime, photoacoustic and ultrasound techniques," Biomed. Opt. Express **4**(9), 1724–1741 (2013).
15. P. Wilder-Smith, W. G. Jung, M. Brenner, K. Osann, H. Beydoun, D. Messadi, and Z. Chen, "In vivo optical coherence tomography for the diagnosis of oral malignancy," Lasers Surg. Med. **35**(4), 269–275 (2004).
16. J. M. Ridgway, W. B. Armstrong, S. Guo, U. Mahmood, J. Su, R. P. Jackson, T. Shibuya, R. L. Crumley, M. Gu, Z. Chen, and B. J. Wong, "In vivo optical coherence tomography of the human oral cavity and oropharynx," Arch. Otolaryngol. Head Neck Surg. **132**(10), 1074–1081 (2006).
17. D. Huang, E. A. Swanson, C. P. Lin, J. S. Schuman, W. G. Stinson, W. Chang, M. R. Hee, T. Flotte, K. Gregory, C. A. Puliafito, and J. G. Fujimoto, "Optical coherence tomography," Science **254**(5035), 1178–1181 (1991).
18. D. Nankivil, A. H. Dhalla, N. Gahm, K. Shia, S. Farsiu, and J. A. Izatt, "Coherence revival multiplexed, buffered swept source optical coherence tomography: 400 kHz imaging with a 100 kHz source," Opt. Lett. **39**(13), 3740–3743 (2014).
19. I. Grulkowski, J. J. Liu, B. Potsaid, V. Jayaraman, J. Jiang, J. G. Fujimoto, and A. E. Cable, "High-precision, high-accuracy ultralong-range swept-source optical coherence tomography using vertical cavity surface emitting laser light source," Opt. Lett. **38**(5), 673–675 (2013).
20. L. An, P. Li, T. T. Shen, and R. Wang, "High speed spectral domain optical coherence tomography for retinal imaging at 500,000 A-lines per second," Biomed. Opt. Express **2**(10), 2770–2783 (2011).
21. M. T. Tsai and M. C. Chan, "Simultaneous 0.8, 1.0, and 1.3 μm multispectral and common-path broadband source for optical coherence tomography," Opt. Lett. **39**(4), 865–868 (2014).
22. M. T. Tsai, H. C. Lee, C. K. Lee, C. H. Yu, H. M. Chen, C. P. Chiang, C. C. Chang, Y. M. Wang, and C. C. Yang, "Effective indicators for diagnosis of oral cancer using optical coherence tomography," Opt. Express **16**(20), 15847–15862 (2008).
23. M. T. Tsai, H. C. Lee, C. W. Lu, Y. M. Wang, C. K. Lee, C. C. Yang, and C. P. Chiang, "Delineation of an oral cancer lesion with swept-source optical coherence tomography," J. Biomed. Opt. **13**(4), 044012 (2008).
24. W. Jung, J. Zhang, J. Chung, P. Wilder-Smith, M. Brenner, J. S. Nelson, and Z. Chen, "Advances in oral cancer detection using optical coherence tomography," IEEE J. Sel. Top. Quantum Electron. **11**(4), 811–817 (2005).
25. C. D. Lu, M. F. Kraus, B. Potsaid, J. J. Liu, W. Choi, V. Jayaraman, A. E. Cable, J. Hornegger, J. S. Duker, and J. G. Fujimoto, "Handheld ultrahigh speed swept source optical coherence tomography instrument using a MEMS scanning mirror," Biomed. Opt. Express **5**(1), 293–311 (2013).
26. H. Pahlevaninezhad, A. M. Lee, T. Shaipanich, R. Raizada, L. Cahill, G. Hohert, V. X. Yang, S. Lam, C. MacAulay, and P. Lane, "A high-efficiency fiber-based imaging system for co-registered autofluorescence and optical coherence tomography," Biomed. Opt. Express **5**(9), 2978–2987 (2014).
27. A. M. Lee, L. Cahill, K. Liu, C. MacAulay, C. Poh, and P. Lane, "Wide-field in vivo oral OCT imaging," Biomed. Opt. Express **6**(7), 2664–2674 (2015).
28. B. Davoudi, A. Lindenmaier, B. A. Standish, G. Allo, K. Bizheva, and A. Vitkin, "Noninvasive in vivo structural and vascular imaging of human oral tissues with spectral domain optical coherence tomography," Biomed. Opt. Express **3**(5), 826–839 (2012).
29. R. Cernat, T. S. Tatla, J. Pang, P. J. Tadrous, A. Bradu, G. Dobre, G. Gelikonov, V. Gelikonov, and A. G. Podoleanu, "Dual instrument for in vivo and ex vivo OCT imaging in an ENT department," Biomed. Opt. Express **3**(12), 3346–3356 (2012).
30. W. Jung, J. Kim, M. Jeon, E. J. Chaney, C. N. Stewart, and S. A. Boppart, "Handheld optical coherence tomography scanner for primary care diagnostics," IEEE Trans. Biomed. Eng. **58**(3), 741–744 (2011).
31. W. J. Choi and R. K. Wang, "In vivo imaging of functional microvasculature within tissue beds of oral and nasal cavities by swept-source optical coherence tomography with a forward/side-viewing probe," Biomed. Opt. Express **5**(8), 2620–2634 (2014).
32. J. Yang, L. Liu, J. P. Campbell, D. Huang, and G. Liu, "Handheld optical coherence tomography angiography," Biomed. Opt. Express **8**(4), 2287–2300 (2017).

Biomedical Optics EXPRESS

33. Z. Ding, Y. Zhao, H. Ren, J. Nelson, and Z. Chen, "Real-time phase-resolved optical coherence tomography and optical Doppler tomography," Opt. Express **10**(5), 236–245 (2002).
34. G. Liu, L. Chou, W. Jia, W. Qi, B. Choi, and Z. Chen, "Intensity-based modified Doppler variance algorithm: application to phase instable and phase stable optical coherence tomography systems," Opt. Express **19**(12), 11429–11440 (2011).
35. L. An, J. Qin, and R. K. Wang, "Ultrahigh sensitive optical microangiography for in vivo imaging of microcirculations within human skin tissue beds," Opt. Express **18**(8), 8220–8228 (2010).
36. R. K. Wang, L. An, P. Francis, and D. J. Wilson, "Depth-resolved imaging of capillary networks in retina and choroid using ultrahigh sensitive optical microangiography," Opt. Lett. **35**(9), 1467–1469 (2010).
37. A. Mariampillai, B. A. Standish, E. H. Moriyama, M. Khurana, N. R. Munce, M. K. Leung, J. Jiang, A. Cable, B. C. Wilson, I. A. Vitkin, and V. X. Yang, "Speckle variance detection of microvasculature using swept-source optical coherence tomography," Opt. Lett. **33**(13), 1530–1532 (2008).
38. M. S. Mahmud, D. W. Cadotte, B. Vuong, C. Sun, T. W. Luk, A. Mariampillai, and V. X. Yang, "Review of speckle and phase variance optical coherence tomography to visualize microvascular networks," J. Biomed. Opt. **18**(5), 50901 (2013).
39. J. Enfield, E. Jonathan, and M. Leahy, "In vivo imaging of the microcirculation of the volar forearm using correlation mapping optical coherence tomography (cmOCT)," Biomed. Opt. Express **2**(5), 1184–1193 (2011).
40. E. Jonathan, J. Enfield, and M. J. Leahy, "Correlation mapping method for generating microcirculation morphology from optical coherence tomography (OCT) intensity images," J. Biophotonics **4**(9), 583–587 (2011).
41. C. H. Yang, M. T. Tsai, S. C. Shen, C. Y. Ng, and S. M. Jung, "Feasibility of ablative fractional laser-assisted drug delivery with optical coherence tomography," Biomed. Opt. Express **5**(11), 3949–3959 (2014).
42. M. T. Tsai, J. W. Zhang, Y. H. Liu, C. K. Yeh, K. C. Wei, and H. L. Liu, "Acoustic-actuated optical coherence angiography," Opt. Lett. **41**(24), 5813–5816 (2016).
43. R. Djaberi, J. D. Schuijf, E. J. de Koning, D. C. Wijewickrama, A. M. Pereira, J. W. Smit, L. J. Kroft, Ad. Roos, J. J. Bax, T. J. Rabelink, and J. W. Jukema, "Non-invasive assessment of microcirculation by sidestream dark field imaging as a marker of coronary artery disease in diabetes," Diab. Vasc. Dis. Res. **10**(2), 123–134 (2013).
44. E. A. Naumova, T. Dierkes, J. Sprang, and W. H. Arnold, "The oral mucosal surface and blood vessels," Head Face Med. **9**, 8 (2013).
45. G. A. Scardina and P. Messina, "Oral microcirculation in post-menopause: a possible correlation with periodontitis," Gerodontology **29**(2), e1045–e1051 (2012).

1. Introduction

Oral cancer has become a severe health problem worldwide, affecting over 325,000 people and causing more than 157,000 deaths in 2015 [1]. Fortunately, with diagnosis and proper treatments in the premalignant conditions or the early-stage oral cancer, the survival rate, on average, can exceed 70%. Generally, an oral mucosa consists of two main layers including the epithelium and lamina propria [2]. In the premalignant stage, the abnormal cells start to emerge from the basal membrane which is the boundary between the epithelium and the lamina propria [3]. Therefore, the symptoms of the morphological change in the epithelium and lamina propria layers can be utilized to detect the premalignant conditions of the oral cavity. Moreover, previous reports have demonstrated that oral premalignant and malignant lesions cause microcirculation changes [4–6]. According to the functionality, oral mucosae can be divided into three types: lining, masticatory, and specialized mucosae. Moreover, lining mucosa includes labial, buccal, and alveolar mucosae. Gingival mucosa belongs to masticatory mucosa, and the dorsal surface of the tongue is a specialized mucosa. However, the morphological and microcirculation features of different mucosal types vary. Therefore, an imaging tool enabling the *in vivo* reconstruction of the microstructure and micro-angiography of various oral mucosal types is highly useful for the diagnosis of oral lesions [7,8].

Currently, different optical imaging methods have been proposed to diagnose oral premalignant/malignant lesions because of their high-resolution and noninvasive natures, such as harmonic [9], multiphoton [10,11], confocal [12,13], photoacoustic [14] microscopies, as well as optical coherence tomography (OCT) [15,16]. For oral cavity imaging with microscopic techniques including harmonic, multiphoton, and confocal microscopies, the penetration depth is limited to hundreds micrometers, which may not be deep enough to investigate the existence of abnormal cells in the premalignant or malignant stage. Moreover, exogenous fluorescence dyes are likely to be required when using confocal

Biomedical Optics EXPRESS

microscopy for microvascular imaging. Although photoacoustic microscopy is a promising label-free method for microvascular imaging, it is difficult to acquire the structural information of the oral mucosa. In addition, the imaging speed of photoacoustic microscopy could be a key issue, making *in vivo* the studies on human subjects challenging. In contrast, it has been proven that using OCT enables *in vivo* imaging of oral mucosa and identification of the morphological changes. The OCT technique was first proposed by D. Huang *et al.* in 1991, using an interferometer to retrieve depth-resolved information [17]. The invention of the Fourier-domain OCT technique, including swept-source OCT (SS-OCT) [18,19] and spectral-domain OCT (SD-OCT) [20,21], greatly improve the system sensitivity and the imaging speed. In our previous studies, the results indicated that OCT can provide high sensitivity and specificity to differentiate various early stages of oral cancer as well as squamous cell carcinoma [22]. Moreover, OCT was used to determine the boundary between normal and cancerous tissue [23]. However, for *in vivo* scanning oral cavity with OCT, a handheld probe is requested. Different OCT handheld probe designs have been proposed. W. Jung *et al.* proposed to use a two-axis MEMS-based scanner to achieve 3D imaging of the oral cavity [24]. C. D. Lu *et al.* developed a handheld ophthalmic instrument based on a 2D MEMS-based mirror [25]. However, the driving voltage of the electrostatic MEMS-based mirror must be greater than tens of volts, which would pose safety concerns for use in endoscopic applications. In particular, the MEMS mirrors are mostly designed in the distal end of endoscopic catheters. Additionally, the implementation of a fiber-optic rotary pullback catheter can effectively minimize the probe size and provides wide-field imaging of oral mucosa [26,27]. Because oral mucosa is not a tubular structure, the acquisition efficiency sine half of the data set was not usable. With rotary and pullback mechanisms, linearity and stability could be major concerns to acquire OCT angiography. In contrast, the galvanometer has become a common solution to provide precise beam scanning because of the high linearity and stability. Using a two-axis galvanometer accompanied by a forehead or chin rest can restrict involuntary movement during OCT measurements [28,29]. W. Jung *et al.* demonstrated a handheld OCT system with a galvanometer-based probe as a point-of-care instrument [30]. The previous study also revealed that a galvanometer-based OCT probe enabled the acquisition of angiography of oral mucosa, nasal cavity, and retina in human subjects [31,32]. Therefore, a two-axis galvanometer was implemented in our handheld probe. Additionally, in previous reports using galvanometers for OCT probe designs, the weight of the scanning probe is an important issue, with the potential to cause motion artifacts during OCT measurement.

Additionally, various OCT-based angiography techniques have been intensively developed including Doppler/Doppler-variance OCT [33,34], optical micro-angiography [35,36], speckle-variance OCT (sv-OCT) [37,38], and correlation-mapping OCT (cm-OCT) [39,40]. In particular, the OCT intensity-based angiographic methods include sv-OCT and cm-OCT, which estimate the intensity variance or cross-correlation between time-variant B-scans obtained at the same location. Such approaches are independent of the phase stability and can be applied for current OCT systems without increasing the complexity of the system setup. In this study, a handheld probe was developed for oral cavity scanning to provide *in vivo* microstructural and microvascular imaging. To reduce the probe weight and simplify the fabrication, the body of the probe was fabricated by a 3D printer to assemble the optical components and the optical scanning device. Additionally, in our design, the distal end of the probe can be switched to fit various oral conditions. Then, an SS-OCT system with the developed probe was used to scan various sites of oral mucosa to *in vivo* investigate the difference in morphology and microcirculation. Here, the 3D angiography was based on the estimation of correlation between inter-frames obtained at the same tissue location. Finally, the different features of various mucosal types were identified and compared.

Biomedical Optics EXPRESS

2. Experimental setup and method

2.1 Design of optical scanning probe

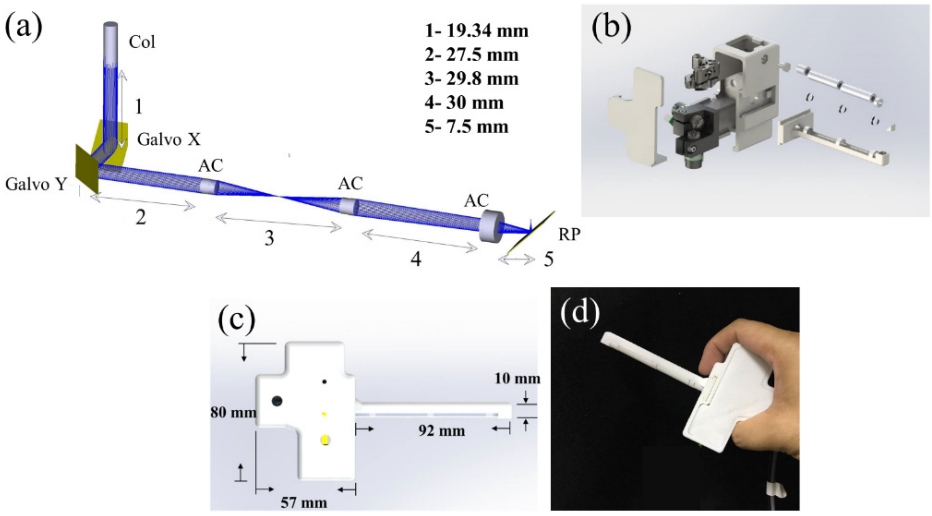

Fig. 1. Design of a handheld probe for oral cavity scanning. (a) Optical path of the probe simulated by Zemax; (b) assembly of the handheld probe; (c) size of probe; (d) probe picture. Col: collimator, Galvo: galvanometer, AC: achromatic lens, and RP: right-angle prism mirror.

The design of an optical scanning probe is an important issue for scanning arbitrary oral mucosal sites. In addition, to reduce unconscious motion artifacts during OCT scanning, an OCT system with a high frame rate is necessary. On the other hand, a probe with a low weight is also effective in reducing motion artifacts induced by the physicians. In this study, the body of the probe was designed using SOLIDWORKS (SolidWorks Corporation, Massachusetts, USA), and the optical path of the probe was simulated using Zemax (ZEMAX LLC, USA). The body was then fabricated by a 3D printer to mount the optical and mechanical components. Figure 1 shows the mechanical and optical layouts of the scanning probe consisting of a probe body, collimator (F028APC, Thorlabs, Inc., NJ, USA), two-axis galvanometer (6200H, Cambridge Technology, MA, USA), three achromatic lenses (AC064-013-C, AC064-013-C, AC064-015-C, Thorlabs, Inc., NJ, USA), and a right-angle prism mirror (MRA05-G01, Thorlabs, Inc., NJ, USA). Figure 1(a) shows the optical layout of the probe. The optical beam from a single-mode fiber was connected to a collimator. Then, the optical beam was incident on the two-axis galvanometer to provide beam scanning along the X and Y directions. Subsequently, the optical beam was incident into the relay lenses, and the beam was focused and reflected by a right-angle reflective prism. Also, the distal end of the probe can be easily switched to meet different clinical requirements. However, the oral cavity is a salivary-rich environment and the mucosal tissue presents a curvature structure, making scanning of the oral cavity challenging. Therefore, we used a plastic membrane attached at the output end of probe that could be replaced after use. In addition, in our probe design, the optical beam was designed to be focused at a depth of 200 μm beneath the tissue surface. Figures 1(b) and 1(c) show the probe layout for the integration of the optical and mechanical components, and Fig. 1(d) shows the photo of the optical scanning probe.

2.2 Setup of SS-OCT system

Figure 2 shows the schematic diagram of the SS-OCT setup which was similar to the setup in the previous study [41]. A MEMS-based swept source (HSL-20, Santec Corp., Japan) centered at 1310 nm provided a scanning speed of 100 kHz with a spectral range of 100 nm.

Biomedical Optics EXPRESS

The SS-OCT system was based on a Mach-Zehnder interferometer which split the light beam into the reference and sample arms. Then, the scanning probe was connected to the sample arm of interferometer. Because the optical components in the reference and sample arms were different, it resulted in redundant dispersion that could degrade the longitudinal resolution of the OCT system. A dispersion compensator was inserted in the reference arm and a software dispersion compensation was implemented to further eliminate the dispersion. Finally, the two light beams from the output ends of the 50/50 fiber coupler were detected by a balanced detector (PDB460C, Thorlabs, Inc., NJ, USA) and digitized by a high-speed digitizer (ATS9350, Alazar Technologies, Inc., Canada). The measured axial and transverse resolutions of the OCT system were approximately 8 and 10 μm, respectively. The physical scanning range of the developed OCT system was 2 × 2 × 2 (mm^3).

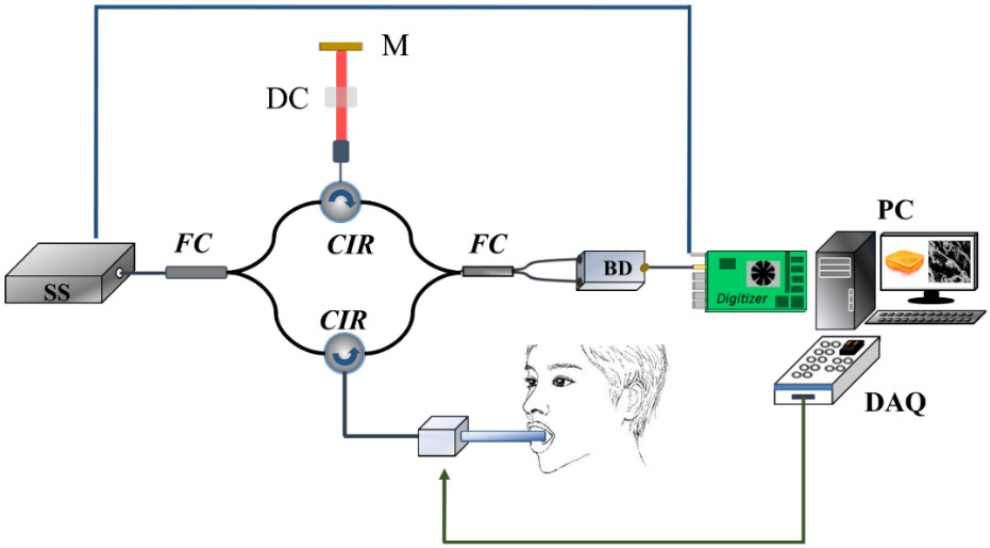

Fig. 2. Schematic diagram of the SS-OCT system. SS: swept-source, CIR: circulator, FC: fiber coupler, DC: dispersion compensator, M: mirror, BD: balanced detector, DAQ: data acquisition board, and PC: personal computer.

In addition, to acquire a micro-angiograph of oral mucosa from the OCT intensity images, the correlation mapping method was implemented in this study [39]. To compare the cross-correlation relationship between the time-variant OCT images obtained at the same location, two sequential B-scans at the same location were performed. Therefore, the fast axis (X) of the galvanometer was driven by a triangular wave to acquire two sequential B-scans at the same location. Then, the correlation coefficient, *Corr*(*x*,*z*), between two B-scans can be estimated as follows:

$$Corr(x,z)=\frac{\sum_{i=1}^{m}\sum_{j=1}^{n}[I_A(x+i,z+j)-\overline{I_A}][I_B(x+i,z+j)-\overline{I_B}]}{\sqrt{\sum_{i=1}^{m}\sum_{j=1}^{n}[I_A(x+i,z+j)-\overline{I_A}]^2\cdot\sum_{i=1}^{m}\sum_{j=1}^{n}[I_B(x+i,z+j)-\overline{I_B}]^2}} \quad (1)$$

where m and n are the grid sizes to obtain an average result and to reduce the noise, respectively [42]. In our study, both m and n were equal to 5. $I_A(x, z)$ and $I_B(x, z)$ are the pixel intensities of two sequential OCT images obtained at the same location. $\overline{I_A}$ and $\overline{I_B}$ are the mean values of each grid. x and z correspond to the locations along the transverse and depth directions, respectively. The other axis of the galvanometer was driven by a step function to

Biomedical Optics EXPRESS

perform the C-scan. To complete 3D micro-angiography, 1000 B-scans were recorded with two repetitions obtained at each location. Therefore, a 3D volume consisted of 1000 (X) × 500 (Y) × 1024 (Z) voxels, which corresponded to a physical size of 2 × 2 × 2 (mm^3). Each 3D image took 10 s, which is acceptable for volunteers to restrain from unnecessary motion.

3. Experimental results

To evaluate the feasibility of the *in vivo* imaging with the developed probe and to identify the microstructural and microvascular features of various oral mucosa sites, different oral mucosal types of healthy volunteers were scanned. The experiments were approved by the Institutional Review Board in Chang Gung Medical Foundation. As mentioned in the introductory section, oral mucosa can be divided into three main types: lining, masticatory, and specialized mucosae. First, the lining mucosae, including the labial and buccal mucosae, were scanned with the developed OCT system. Figure 3 shows *in vivo* OCT images of the upper lip obtained from a healthy 24-year-old male volunteer. Figures. 3(a) and 3(b) are the 2D and 3D OCT images of the labial mucosa, respectively, in which the epithelium and lamina propria layers can be clearly identified along with a salivary gland, as indicated by the white arrow in Fig. 3(a). The strong backscattered signal, indicated by the white arrow in Fig. 3(b), was due to the strong reflection from the plastic membrane used for preventing the optical components in the probe from being polluted by saliva. Figure 3(a) also illustrated that the lamina propria layer showed a stronger backscattered intensity than the epithelial layer. Figures. 3(c)–3(h) show the maximum intensity projection of angiographies at varying depths of 300–310, 350–360, 400–410, 450–460, 500–510, and 300–600 μm, respectively. The results showed that the vessels existed in the lamina propria layer and the sizes of the vessels were smaller in the shallower depth range. For the labial mucosa, the capillaries showed a tortuosity as indicated by the loop structures from the arterioles [43,44], which were also observed in the OCT angiographic images as specified by the yellow arrows in Fig. 3(f). In general, the majority of the capillary tortuosity was categorized by five types according to the number of twists (from zero to four twists). Additionally, Figs. 3(c)-3(h) illustrated the microcirculation of labial mucosa, showing a hairpin-shaped conformation in the shallow depth that was coincident with the results of the previous report [45]. Additionally, such capillary tortuosity in the labial mucosa can be altered by diseases, and the visualization of the capillary tortuosity could be an important tool for early diagnosis.

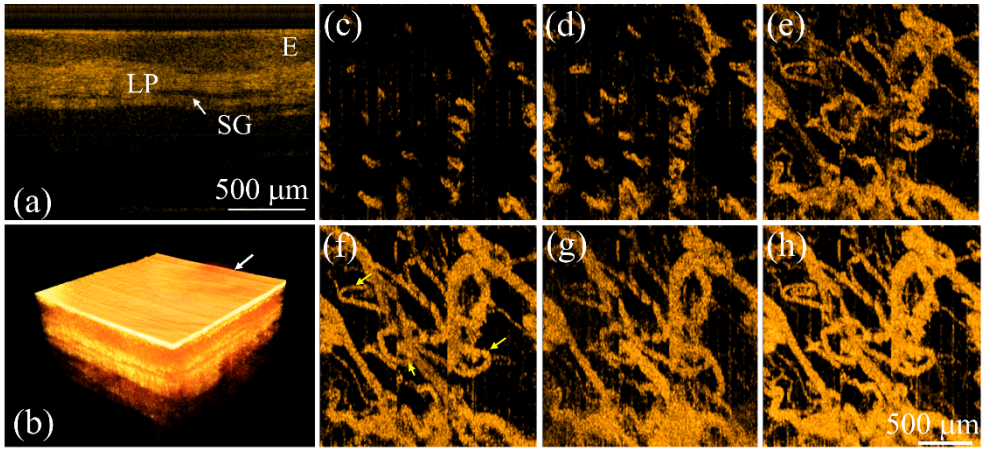

Fig. 3. *In vivo* OCT images of the upper lip obtained from a healthy 24-year-old male including a (a) 2D image, (b) 3D image, and (c)–(h) projection-view angiographies obtained at varying depths of 300–310, 350–360, 400–410, 450–460, 500–510, and 300–600 μm, respectively, beneath the lip surface. E: epidermis, LP: lamina propria, and SG: salivary gland. The scale bar in (a) represents 500 μm. The yellow arrows indicate the twists of capillaries.

Biomedical Optics EXPRESS

Moreover, the average vessel diameter and vessel density in Figs. 3(c)–3(g) were estimated and reported in Fig. 4. Twenty different vessel locations were randomly selected in each angiographic image, allowing a manual estimation of the average vessel diameter accordingly. As shown in Fig. 4(a), the estimated average vessel diameters were 48, 59, 69, 73, and 83 μm, respectively, indicating the vessel diameter increased with the depth. In addition, for the estimation of the vessel density, each angiographic image was thresholded to reject areas with low OCT angiographic signal intensities (for example, background noise). In each angiographic image, the threshold value was determined by averaging the OCT angiographic signal intensities over the entire angiographic image. Then, areas with OCT angiographic signal intensities higher than the threshold value were summed and divided by the area of the entire OCT angiographic image afterward to estimate the average vessel density. Figure 4(b) shows the results of the estimated average vessel densities of Figs. 3(c) – 3(g). Similar to the trend observed in Fig. 4(a), the average vessel density also increased with depth.

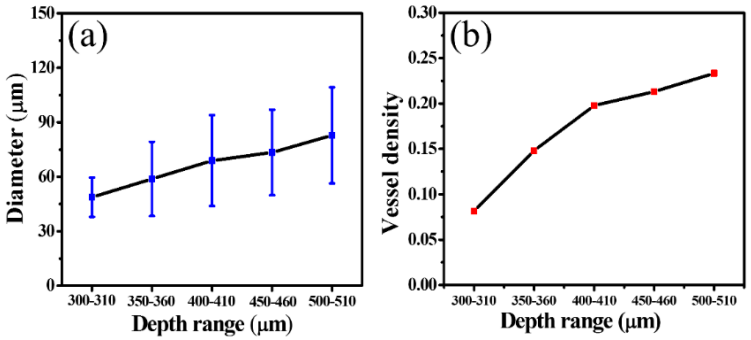

Fig. 4. Estimated results of (a) the averaged vessel diameters and (b) the vessel densities of Fig. 3(c)-3(g).

Subsequently, the buccal mucosa of a healthy 25-year-old female was scanned with the developed OCT system. Here, buccal mucosa also belongs to the lining mucosa. Figure 5 shows the 2D OCT, 3D OCT, and projection-view OCT angiographic images of the buccal mucosa. Similar to the results of Fig. 3, two main layers including the epithelium and lamina propria were distinguished, and the epithelial layer showed a weaker backscattering property than that of the lamina propria layer. Similarly, the salivary gland was also found as indicated by the white arrows in Fig. 5(a). Figures 5(c)–5(h) show the representative projection-view OCT angiographies at varying depths. In the same way, capillaries of the buccal mucosa also showed a twist feature as indicated by the yellow arrows. Here, the OCT angiography in Fig. 5 shows a similar microvascular network as Fig. 3, including the capillary tortuosity and the hairpin-shape conformation, due to the lining mucosal type.

Biomedical Optics EXPRESS

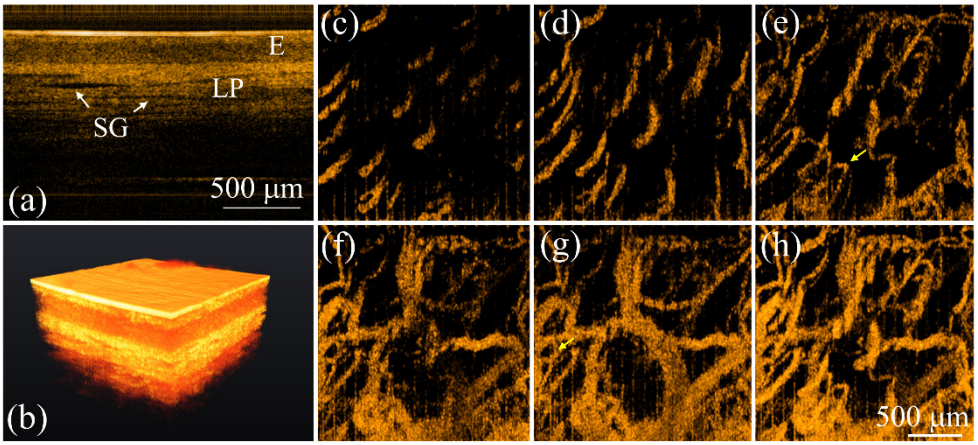

Fig. 5. *In vivo* OCT images of the right buccal mucosa obtained from a healthy 25-year-old female including a (a) 2D image, (b) 3D image, and (c)–(h) projection-view angiographies obtained at varying depths of 250–260, 300–310, 350–360, 400–410, 450–460, and 250–500 μm, respectively, beneath the buccal surface. E: epidermis, LP: lamina propria, and SG: salivary gland. The scale bar in (a) represents 500 μm.

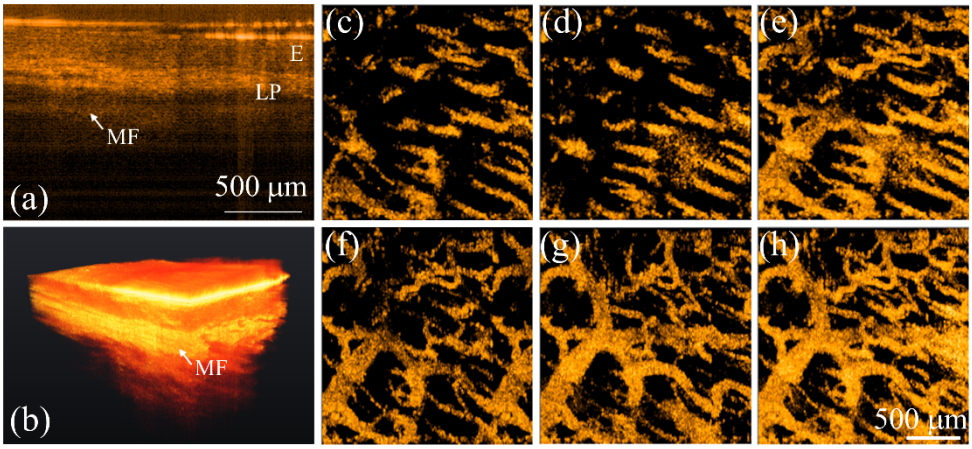

Fig. 6. *In vivo* OCT images of the ventral surface of a tongue obtained from a 25-year-old male including a (a) 2D image, (b) 3D image, and (c)–(h) projection-view angiographies obtained at the various depths of 250–260, 300–310, 350–360, 400–410, 450–460, and 250–500 μm beneath the tongue surface. E: epidermis, LP: lamina propria, and MF: muscle fiber. The scale bar in (a) represents 500 μm.

Then, the ventral surface of the tongue of a healthy 25-year-old male was scanned with OCT, and Fig. 6 shows the OCT results of the ventral tongue. Figures. 6(a) and 6(b) show the representative 2D and 3D OCT images and Figs. 6(c)–6(h) represent the projection-view angiographies at the various depths of 250–260, 300–310, 350–360, 400–410, 450–460, and 250–500 μm, respectively. Here, the ventral tongue included epithelium, lamina propria, and submucosa layers, and the epithelial layer of the ventral tongue was a non-keratinized and stratified structure. The submucosa layer consisted of extremely dense muscle fibers to interlace connective tissue fibers as indicated by the white arrows in Figs. 6(a) and 6(b).

Biomedical Optics EXPRESS

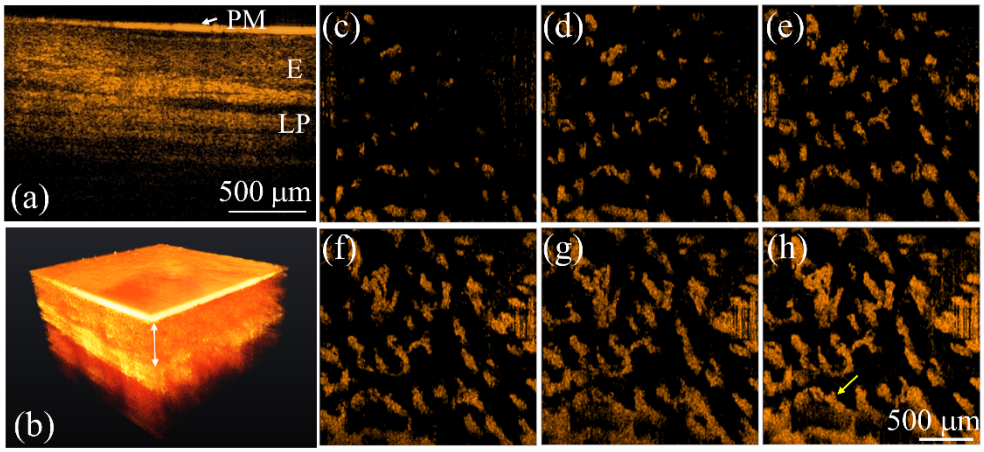

Fig. 7. *In vivo* OCT images of gingival mucosa obtained from a 24-year-old female including a (a) 2D image, (b) 3D image, and (c)–(h) projection-view angiographies obtained at the various depths of 250–260, 300–310, 350–360, 400–410, 450–460, and 250–500 μm beneath the tissue surface. E: epidermis, LP: lamina propria, and PM: plastic membrane. The scale bar in (a) represents 500 μm.

Aside from investigating the microstructural and microvascular features of lining mucosa, the masticatory and specialized mucosae were scanned with OCT. The masticatory mucosa can be found on the gingiva. Therefore, the gingival mucosa of a healthy 24-year-old female was scanned with OCT. Figures 7(a) and 7(b) represent the 2D and 3D OCT images, and Figs. 7(c)–7(h) show the OCT angiographies at the various depths of 250–260, 300–310, 350–360, 400–410, 450–460, and 250–500 μm, respectively, beneath the mucosa surface. Again, the epithelium and laminar propria layers were differentiated as shown in Fig. 7(b), in which the weaker backscattered intensity represented the epithelium and the lamina propria layer resulted in stronger backscattered intensity. The previous report indicated that the epithelium thickness of the gingival mucosa is statistically greater than that of lining mucosa resulting from the keratin structure, which is also indicated by the white arrow in Fig. 7(b) [45]. The function of such keratinized mucosa can resist friction and prevent bacterial invasion. Moreover, compared with other hard keratin tissues such as nails and hairs, gingival mucosa has a softer texture. Additionally, the results of Figs. 7(c)–7(h) illustrate the twists of the capillaries, as indicated by the yellow arrow.

Moreover, compared with the lining and masticatory mucosae, the dorsal surface of the tongue is a type of specialized mucosa that contains nerve endings for taste perception and sensory reception. The dorsal surface of the tongue can be divided into three regions, namely filiform, fungiform, and circumvallate papillae. Here, the fungiform papilla of a healthy 24-year-old male was scanned with OCT and the results are shown in Fig. 8. During our measurement, the tongue was pulled out and fixed by the physician's hand to reduce unconscious motion. This process is commonly performed for visual inspection or treatment in clinical practice. These results differed from those of the other mucosal types, as the dorsal surface of the tongue showed a thin non-keratinized and stratified epithelium as shown in Fig. 8(a). Figure 8(b) shows an *in vivo* 3D OCT image of the dorsal tongue and Fig. 8(c) shows the top-view image of Fig. 8(b) after the removal of the plastic membrane signal, enabling the visualization of the fungiform papilla distribution. For the fungiform papilla, dense twists of vessels beneath the epithelium, were observed and are indicated by the yellow arrows in the OCT angiographic results. However, the fungiform papilla also restricted the backscattered intensity, limiting the effective imaging depth of the OCT angiography.

Biomedical Optics EXPRESS

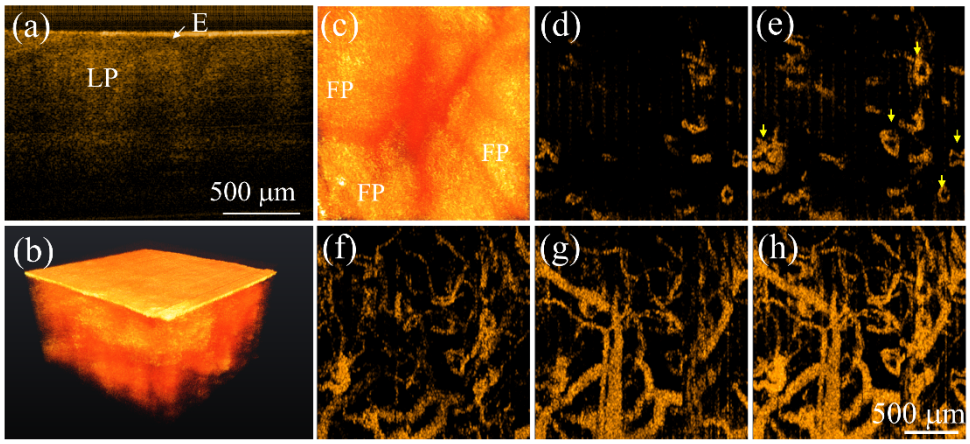

Fig. 8. *In vivo* OCT images of the dorsal surface of a tongue obtained from a 24-year-old male volunteer including a (a) 2D image, (b) 3D image, (c) top-view of 3D image, and (d)–(g) angiographies obtained at the various depths of 200–250, 250–300, 300–350, 350–400, and 200–400 μm beneath the tissue surface. E: epidermis, LP: lamina propria, and FP: fungiform papilla. The scale bar in (a) represents 500 μm in length. The yellow arrows indicate the dense twists of vessels beneath the epithelium.

4. Discussion and conclusion

Previous studies have demonstrated that OCT structural images can be used for oral cancer diagnosis and differentiation of various oral precancerous stages. Because of the development of OCT-based angiographic techniques, OCT can simultaneously provide label-free microcirculation without extra contrast agents or fluorescence dyes. However, the probe design of the OCT system for oral cavity scanning is a key issue. In previous reports, the probe size was miniaturized using a fiber-optic rotary catheter or a MEMS-based scanner. It is difficult to scan the exact same location of biological tissue with a rotary catheter making OCT intensity-based angiographic imaging difficult, resulting in a too poor phase stability to estimate the flow velocity. For MEMS-based scanners, a higher driving voltage is required, causing a safety concern when the probe is used for clinical trials. In this study, we used a miniaturized galvanometer to enable optical scanning along the transverse and lateral directions. The driving voltage was 23 VDC and it was implemented in the proximal end of the probe away from biological tissue. To reduce the probe weight, the probe body was fabricated by a 3D printer that enabled the effective reduction of involuntary motion during OCT measurement. When oral mucosa was scanned with the OCT, a plastic membrane was attached to the output end of the probe, thus preventing pollution from saliva. Moreover, the reduction of stronger backscattered signals from the mucosa surface was achieved because the plastic membrane directly contacted and flattened the tissue surface. Additionally, in our design, the distal end of the probe can be switched to fit various oral conditions, and the optical parameters of the probe, such as the transverse resolution, working distance, and probe length can be easily varied. The relay lenses enabled the extension of the optical beam into the inner region of the oral cavity for the OCT imaging. The total length of the relay lenses also can be further extended by changing the composition of the lenses, enabling an increase of the measureable range in the oral cavity. Furthermore, the current transverse resolution of the OCT system is not good enough to clearly observe the smaller vascular twists. However, the transverse resolution can be further improved by utilizing a focus lens of the probe with a higher numerical aperture. Moreover, the image quality can be further improved by utilizing multiple sequential B-scans when a swept source with a higher A-scan rate is implemented. Additionally, it may be a challenge for scanning tongues due to involuntary motion. The motion artifacts can be further reduced by increasing the imaging speed. The frame rate of our

Biomedical Optics EXPRESS

system was 100 frames/s, which could be further increased by using a Fourier-domain mode locking laser or VCSEL-based swept source as the OCT light source.

Finally, the developed OCT system was implemented for the visualization of various types of oral mucosae including lining, masticatory, and specialized mucosae. From the results, the different structures of oral mucosa were identified, such as the epithelium, lamina propria, salivary gland, and fungiform papilla. Aside from the reconstruction of microstructures of oral mucosa, the developed system simultaneously acquired a micro-angiography of oral mucosa that could be potentially useful as a diagnostic indicator for oral cancer in the early stages. In conclusion, the developed handheld OCT system has been demonstrated for *in vivo* oral cavity imaging, enabling the identification of the different structures and observation of the microcirculation features of various oral mucosal types. This design has potential in applications for the diagnoses of oral diseases and lesions.

Funding

The authors acknowledge partial financial support from the Ministry of Science and Technology of the Republic of China (ROC), Taiwan (MOST 104-2221-E-182-027-MY2 and MOST 105-2221-E182-016-MY3, and MOST 105-2627-M-007-009) and Chang Gung Memorial Hospital, Taiwan (CIRPD2E0041 and CIRPD2E0042).

Disclosures

The authors declare that there are no conflicts of interest related to this article.